#24-017
2024 AFS Proceedings ©American Foundry Society

Cooling Curves of Concentrated Alloys, Steelmaking Slag, and Lithium Iron Phosphate

Delin Li
CanmetMATERIALS, Natural Resources Canada, Hamilton, Ontario, Canada

ABSTRACT

Over the past few years, a variety of melting/casting projects have been performed, in collaboration with industries and universities. Concentrated alloys and nonmetallic compounds were studied including high-Si cast iron, high-Mn steel, Al-added stainless steel, high-entropy alloy, Permalloy 80 Ni alloy, Stellite Co alloy, steelmaking slag and lithium iron phosphate (LFP). A melt synthesis of LFP was developed. Cooling curves were measured using the thermal analysis cup method and differential thermal analysis. In addition, the phase diagrams of alloys were calculated using Thermo-Calc. This paper draws on some examples of the measured cooling curves to illustrate the thermal behaviors of melts, along with a quick review of each project.

Keywords: cooling curves, high-Si iron, high-Mn steel, Al-added stainless steel, high-entropy alloy, Stellite, Permalloy 80, steelmaking slag, and LFP

INTRODUCTION

Thermal analysis (TA) and cooling curves (CC) can be used in many ways and are often used to determine the liquidus and solidus temperatures which are helpful to improve the metalcasting process.[1] There have been immense research and applications of TA for cast iron,[2] low alloy steel[3] and aluminum alloys.[4] However, few reports are available about the cooling curves of concentrated alloys and nonmetallic materials.

In recent years, various experiment studies have been performed in CanmetMATERIALS, including high-Si cast iron, high-Mn steel, Al-alloyed stainless steel, high-entropy alloy (HEA), Permalloy 80 Ni alloy, Stellite Co alloy, steelmaking slag, and lithium iron phosphate (LFP). Cooling curves were measured using the TA cup method during the melting/casting experiments. $LiFePO_4$ is a promising cathode material for lithium-ion battery. It is commercially produced mainly using two methods, solid-state and hydrothermal processes. A novel melt synthesis of LFP has been developed to reduce cost.[5,6] This paper presents the measured cooling curves and calculated phase diagrams, together with a quick introduction of each project.

EXPERIMENTAL PROCEDURES

An induction furnace of 100 kW was utilized with a crucible of 200 mm (8 in.) diameter and 50 kg (110 lb) steel capacity. The SPAL (Surface Protection Air Liquid) lance was installed on the furnace, as shown in Fig. 1. The liquid argon stream from SPAL was applied prior to incipient melting and was maintained throughout the melting/casting cycle. The melt was scooped from furnace or ladle to pour the TA cups, as shown in Fig. 2. Two types of TA cups were utilized, S-type and K-type thermocouples. The dimensions of TA cup are 38 mm (1.5 in.) ID or side length and 38 mm (1.5 in.) depth. DTA (Differential Thermal Analysis) testing was conducted on some of cast samples. The DTA standard procedures were described in a website.[7] The materials studied in this work are summarized in Table. 1.

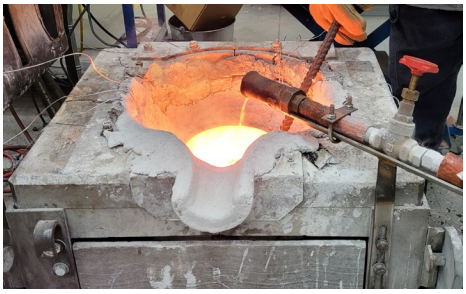

Figure 1. Melting experiments using 100-kW induction furnace with SPAL (Surface Protection Air Liquid) lance installed.

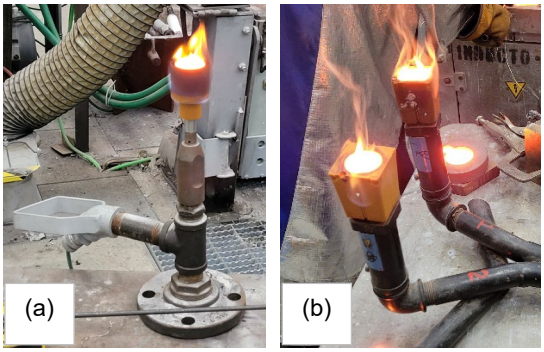

Figure 2. Measurements of cooling curves using the TA cup method: (a) S-type, and (b) K-type cups.

Table 1. Materials Studied in This Work

Mater. ID	Material Type, Formula, and Composition (wt.%)	Ref.
Hi-Si	High-Si Cast Iron in ASTM A518 and Modified: 14.5Si, 0.9C, 0.5Mn, 0 and 5.0Cu.	8
Hi-Mn	High-Mn Steel in ASTM A128: 18.0Mn, 2.0Cr, 1.2C, 0.5Si.	9
Al-St	Al-added Stainless Steel: 0 to 5.5Al, 25Ni, 20Cr, 0.9Si, 0.9Mn, 0.1C.	10
$Ni_{2.1}$	Eutectic HEA, $AlCoCrFeNi_{2.1}$: 8.5Al, 18.6Co, 16.4Cr, 17.6Fe, 38.9Ni.	11
Ni80	ASTM A753, Type 4 Permalloy 80: e.g., 80Ni, 15Fe, 5Mo.	12
SF12	Cobalt-base Alloy, Stellite: 19Cr, 14Ni, 9W, 3Si, 2Fe, 2B, 0.9C.	13
Slag	EAF Steelmaking Slag: e.g., 38CaO, 25FeO, $14SiO_2$, 10MgO, $6Al_2O_3$, 6MnO.	14
LFP	Li-ion Battery Cathode Material, Lithium Iron Phosphate, $LiFePO_4$.	5, 6

RESULTS AND DISCUSSION

HIGH SILICON CAST IRON

Recently, a critical minerals strategy was announced.[15] It was reported that sulfuric acid roasting was a major decomposition process of rare earth concentrate, which is commercially practiced in a rotary kiln (RK).[16] The liner wall of the RK is susceptible to elevated-temperature acid corrosion, thus a very short life. Hi-Si iron could be one of candidates for the liner material in a RK. It is a special iron for corrosion resistant applications, which contains up to 14-18% Si (composition in wt.% was used throughout this paper) in the ASM handbook[17] and ASTM standards A518 and A861. We cast Keel-block castings of 24 × 170 mm (1 × 7 in.) using no-bake sand molds for material and process evaluations. The alloys were poured at ~1345C (2455F). In-mold inoculant of 0.07% FeSi (Elkem) was added. Two compositions of samples were cast per ASTM A518: melt 1A (Grade 1, 14.5% Si), and melt 1B (Grade 1 plus 5% Cu and 0.05% rare earth mainly Ce). The chemical compositions were analyzed using OES (Optical Emission Spectrometry), XRF (X-ray Fluorescence), and ICP-AES (Inductively Coupled Plasma-Atomic Emission Spectroscopy). The mechanical and corrosion properties of Hi-Si cast iron were improved by the additions of copper and rare earth.[18] The thermal arrests in Figs. 3 and 4 can be found to estimate the liquidus T_L and solidus T_S temperatures, because of low undercooling and cooling rate usually occur in the TA cup samples.

The T_L and T_S (eutectic plateau) of melt 1A was determined as 1190C (2175F), and 1180C (2155F), respectively from the measured curves, which agrees with the calculated phase diagram in Fig. 5(a). The comparison of the phase diagrams Figs. 5(a) and (b) shows that the additions of 5% Cu and 0.05% Ce (melt 1B) reduced the eutectic carbon content by 0.1% C and increased the eutectic temperature T_E by 10°C (20°F). In contrast to the calculations, the measured T_E of melt 1B was decreased by 15°C (30°F) as compared to melt 1A, as shown in Fig. 3. This can be due to the Ce-induced undercooling which is not reflected in the equilibrium phase diagrams. Formation of chunk graphite shown in Fig. 6(b) can be a sign of undercooled melt 1B.

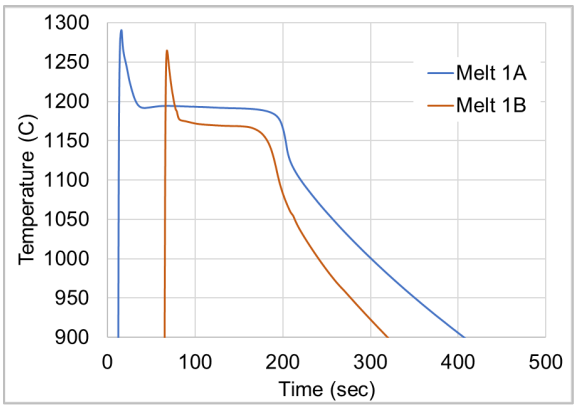

Figure 3. Measured cooling curves of 14.5% Si iron: melt 1A and melt 1B (plus 5% Cu and 0.05% Ce).

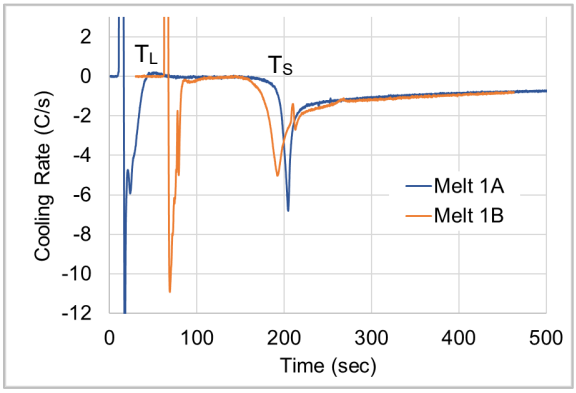

Figure 4. Cooling rates of melt 1A and melt 1B.

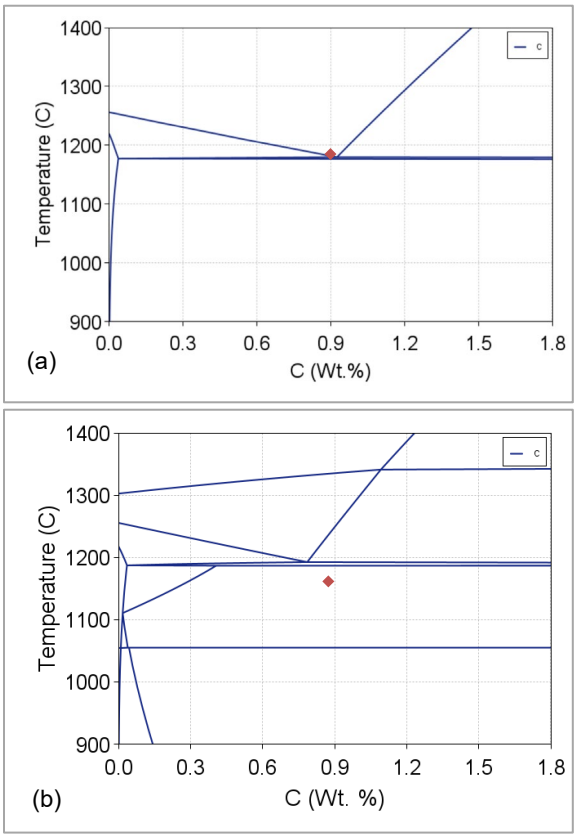

Figure 5. Calculated phase diagrams of Hi-Si iron with CC measurements (dots): (a) melt 1A, and (b) melt 1B.

Type A graphite flakes are randomly distributed and oriented throughout the samples of melt 1A, as shown in Fig. 6(a). The flake graphite was transformed to chunky graphite (Fig. 6b) due to the addition of Ce. The Cu-rich phase was formed in melt 1B. The 14.5% Si iron is much more susceptible to gas porosity defects than other iron castings of lower Si, e.g., 4.5% Si iron. Material testing including corrosion in concentrated H_2SO_4 is underway.

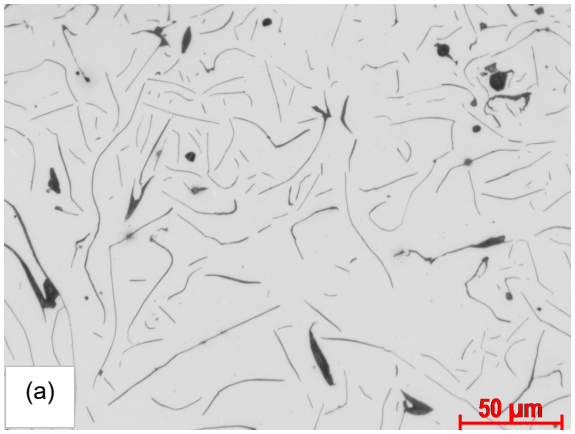

Figure 6. Micrographs of 14.5% Si iron samples: (a) melt 1A. view (b) in next column.

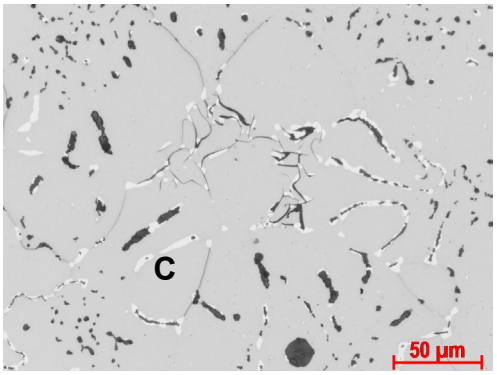

Figure 6. (cont.) Micrographs of 14.5% Si iron samples: (b) melt 1B showing modified graphite shapes and Cu-rich phase (marked "C").

HIGH MANGANESE STEEL

High-Mn steel castings, or Hadfield steel, with12 - 22% Mn, 1.0 - 1.5% C are widely used as critical components in cement, mining, and construction operations due to their excellent wear resistance, work hardenability, and formability.[9] Although 10 grades of austenitic Mn steel are identified in ASTM standard A128, continuous research work has been caried out, e.g., adding alloying elements Al, Cr, Mo, Ti, and V.[19] Some producers had their success in implementing the various grain refinement techniques, but the most reliable method to obtain a fine grain structure is to pour the metal with low superheat.[19] The recommended pouring temperature was 1400C (2550F). The TA cups samples were poured to obtain the cooling curves of Hi-Mn samples (Fig. 7). Because of low pouring temperatures, the superheated stage of liquid steel was missed out for the cooling curves except curve #5 (Fig. 7). The T_L of the 18% Mn steel samples was determined as 1360C (2480F) from the cooling curves. This is close to the calculated T_L from the phase diagram at 1.2% C (Fig. 8). Heat treatment of the Hi-Mn castings was conducted per ASTM A128.

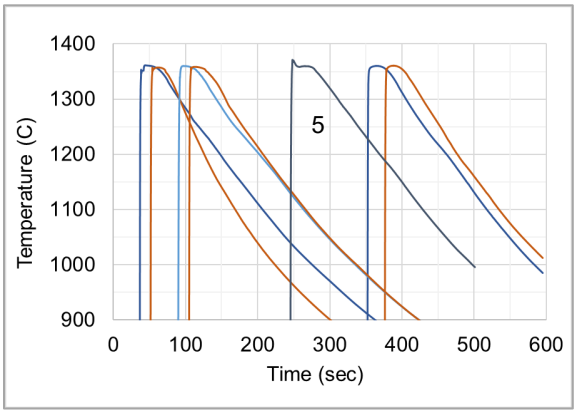

Figure 7. Measured cooling curves of Hi-Mn steel obtained from 7 TA cup samples.

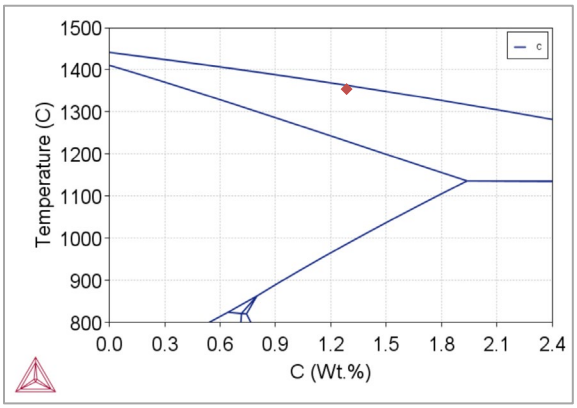

Figure 8. Calculated phase diagram of Hi-Mn steel with CC measurements (red dot).

ALUMINUM-ALLOYED STAINLESS STEEL

The objective of this project was to produce lighter, cleaner, and more heat-resistant steel castings through development of vacuum molding (V-process) and Al-alloyed stainless steel. The V-process can offer several benefits such as using unbonded sand, improving mold filling ability and casting surface finish. Two runner, Y-shaped exhaust manifolds were designed for the V-process experiments as shown in Fig. 9. Al-alloyed steels and irons have long been recognized as very attractive materials due to heat resistance and lightweight high strength. In this work, stainless steel castings (20Cr-25Ni) were made with the Al contents ranging from 0 to 5.5%. The T_L temperatures were decreased by increasing the Al content up to 4.5% Al, as shown in Figs. 10 and 11. When Al exceeds 4.5%, the primary solidification transition occurs from FCC austenite to BCC ferrite (Fig. 11).

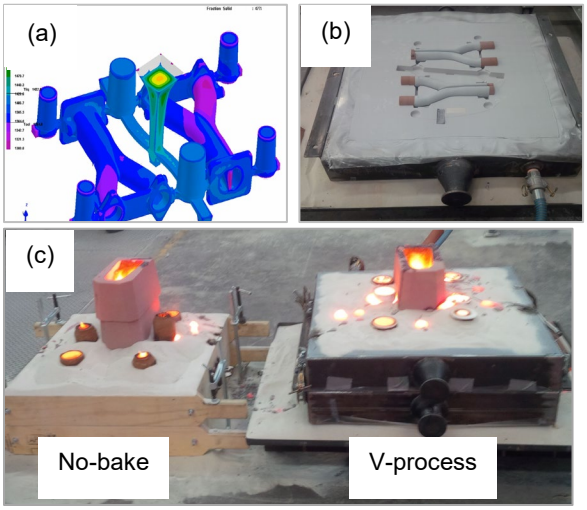

Figure 9. Casting experiments of Y-shaped manifolds using the V-process: (a) simulation of flow and solidification, (b) V-process mold showing vacuum hose and plastic film adhesion, and (c) no-bake and V-process molds for comparison.

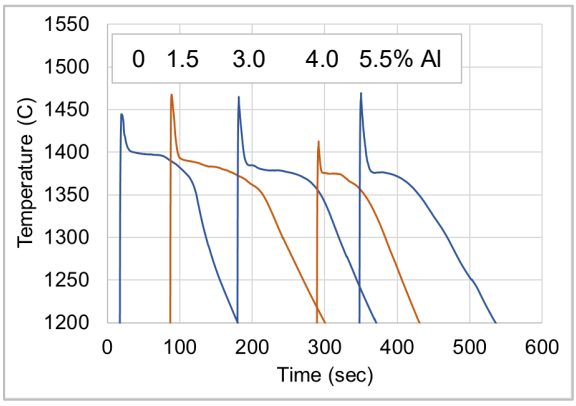

Figure 10. Measured cooling curves of Al-St (Al-added stainless steel) samples with Al contents ranging from 0 to 5.5%.

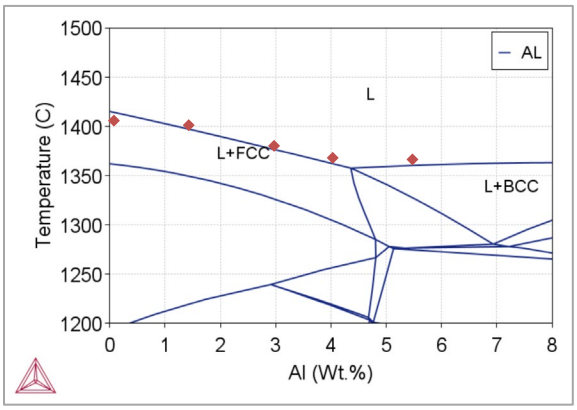

Figure 11. Calculated phase diagram of Al-St with CC measurements (dots).

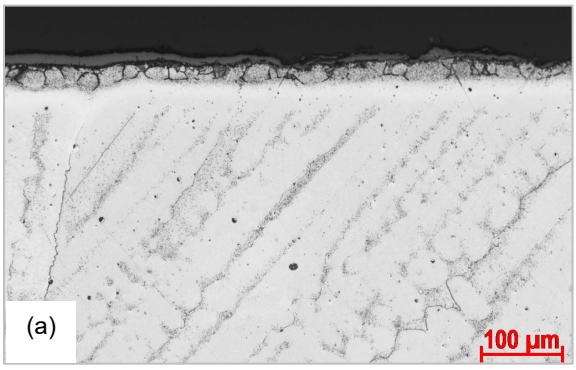

Figure 12. Micrographs of Al-St samples tested at 1000c (1830f) – 400 hrs: (a) 0% Al, (b) 4.0% Al with austenitic matrix. Views (b) and (c) on next page.

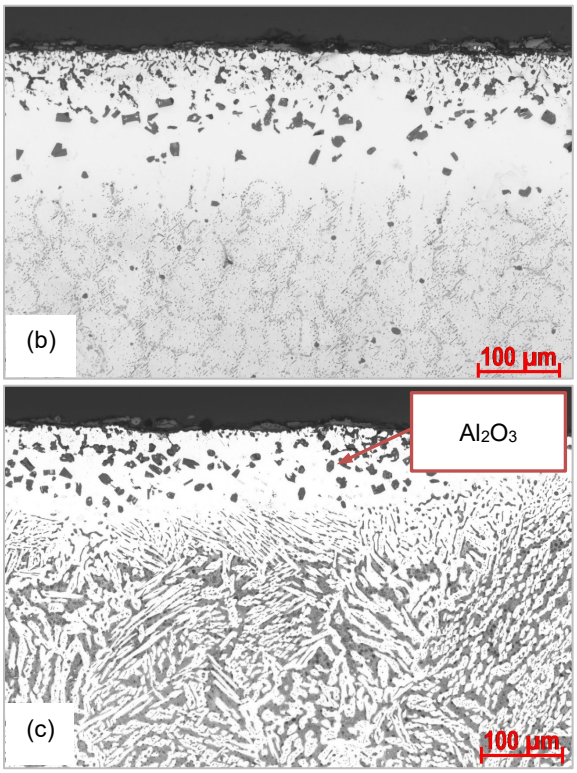

Figure 12. Micrographs of Al-St samples tested at 1000C (1830F) – 400 hrs: (a) previous page (b) 4.0% Al with austenitic matrix, and (c) 5.5 % Al with primary ferrite.

Oxidation testing at 1000C (1830F) was conducted for the Al-St (Al-added stainless steel) samples which were daily removed from a muffle furnace, weighed, and returned to the furnace. Figure 12 shows the micrographs of tested samples. Evident oxide spallation occurred during the testing for the samples of < 4% Al, as also indicated by the broken oxide scales in Fig. 12(a). The Al-St samples of 4.0 and 5.5% Al formed with Al_2O_3 particles adjacent to the surface as shown in Figs. 12(b) and (c), thus greatly enhancing the hot oxidation resistance. The samples of ≧ 4.0% Al consist of austenitic structure. However, ferrite was solidified as a primary phase for the 5.5% Al sample (Fig. 12c), which explains a huge increase in the Brinell hardness (10 mm/ 3000 kg), as listed in Table 2. The Al content should be controlled < 4.5% if a fully austenitic structure is required for the Al-St (Fig. 11). Dross formation of Al-alloyed steel or iron can be a concern during melting and casting.

Table 2. Hardness and Structure of Al-St Samples

% Al	0	1.5	3.0	4.0	5.5
Hardness (HBW)	140	140	135	150	280
Primary Phase	Austenite				Ferrite

EUTECTIC HIGH-ENTROPY ALLOY

Casting, forging, and rolling of HEA was reported where a separate melting method was developed to produce Al-contained HEA.[20] Measured cooling curves are shown in Fig. 13. The T_L (1410C, 2570F) and eutectic temperature T_E (1338C, 2440F) determined from Fig. 13 agree well with the calculated phase diagram in Fig. 14 at the Al content of 8.5% for the HEA $AlCoCrFeNi_{2.1}$. This HEA formula appears to be hypereutectic composition according to the calculations (Fig. 14), which is also supported by the microstructure consisting of primary dendrite phase and lamellae eutectic as shown in Fig. 15. The Al content can be slightly reduced in the HEA $Ni_{2.1}$ formula if aiming at a fully eutectic microstructure.

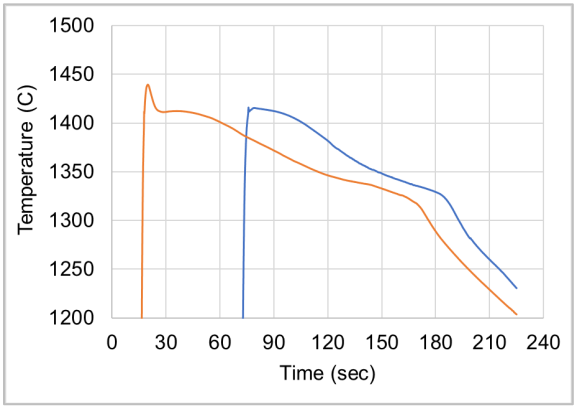

Figure 13. Measured cooling curves of eutectic HEA $AlCoCrFeNi_{2.1}$ obtained from 2 TA cup samples.

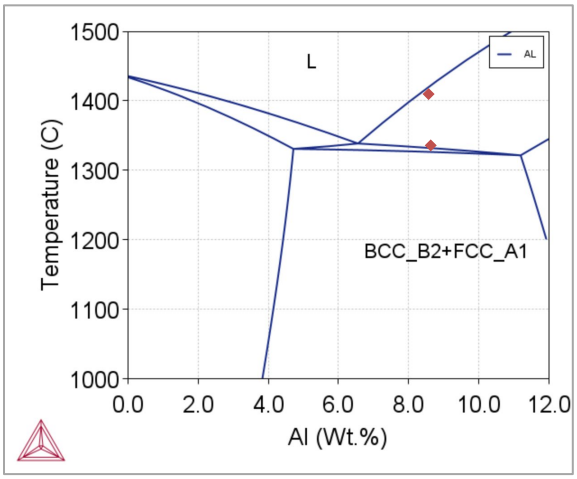

Figure 14. Calculated phase diagram of HEA $AlCoCrFeNi_{2.1}$ with CC measurements (dots).

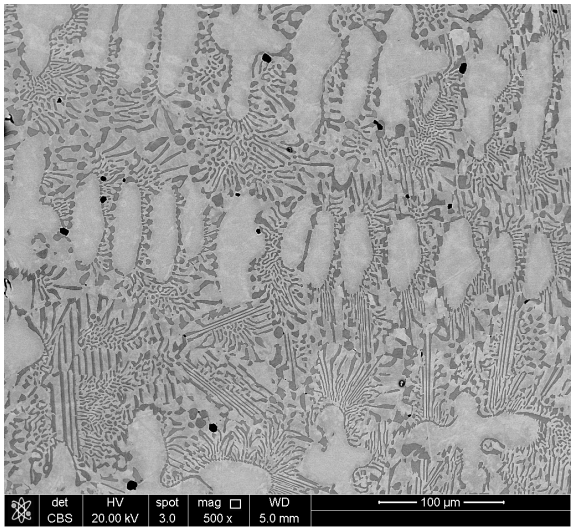

Figure 15. SEM micrograph of cast HEA $AlCoCrFeNi_{2.1}$ sample showing primary dendrite phase and lamellae eutectic microstructure.

PERMALLOY 80

Permalloy 80 (ASTM A753 Type 4) is a highly magnetic nickel-iron-molybdenum alloy, with roughly 80% Ni, 15% Fe and 5% Mo. Permalloy 80 provides high initial and maximum permeabilities with low coercive force, hysteresis loss, eddy-current loss, and magnetostriction, which is critical for industrial applications.[12] The Canmet lab was requested to cast Permalloy 80 ingots. The measured cooling curves are displayed in Fig. 16. Both the measured cooling curves in Fig. 16 and the calculated phase diagram in Fig. 17 show the liquidus temperature of 1428C (2600F). Severe gas porosity defects occurred in the Ni80 castings made from air melts. Finally, quality ingots of Permalloy 80 have been produced using Canmet vacuum induction melting furnace.

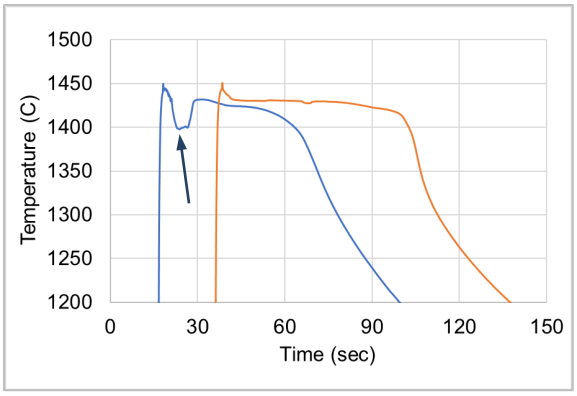

Figure 16. Measured cooling curves of Permalloy 80 obtained from 2 TA cup samples. The curve notch pointed by an arrow is artificial.

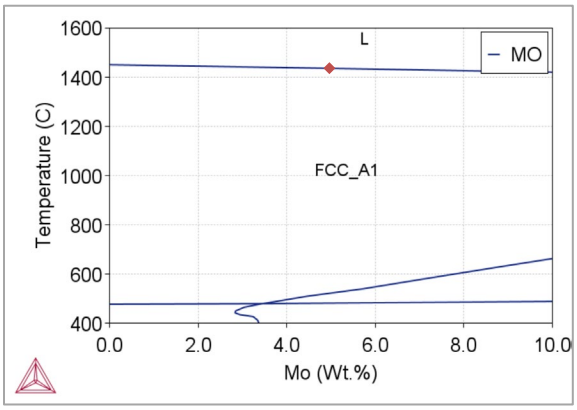

Figure 17. Calculated phase diagram of Permalloy 80 with CC measurements (dot).

COBALT-BASE ALLOY STELLITE

Stellite cobalt-based alloys consist of complex carbides in an alloy matrix. They are resistant to wear, galling, and corrosion and retain these properties at high temperatures. Their exceptional wear resistance is due mainly to the unique inherent characteristics of the hard carbide phase dispersed in a CoCr alloy matrix.[13] The objective of this project is to study the formation of amorphous Stellite (SF12) alloy using gas atomization.[21] SF12 master alloy from Kennametal (Ontario) was melted and cast into small samples in the Canmet lab. Then the small samples were provided to University of Alberta for gas atomization experiments where SF12 amorphous droplets were produced.[21] The T_L of 1190C (2175F) determined from the cooling curves in Fig. 18 and phase diagram in Fig. 19 are reasonably close to each other. The thermal arrests at 1100C (2010F) in the cooling curves (Fig. 18) may correspond to the peritectic transformation shown in the phase diagram in Fig. 19.

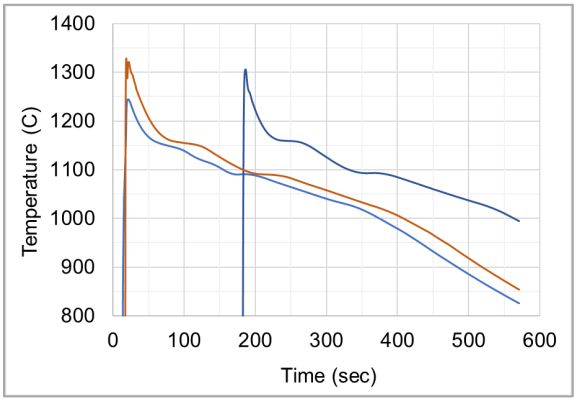

Figure 18. Measured cooling curves of Stellite SF12, Co-base alloy obtained from 3 TA cup samples.

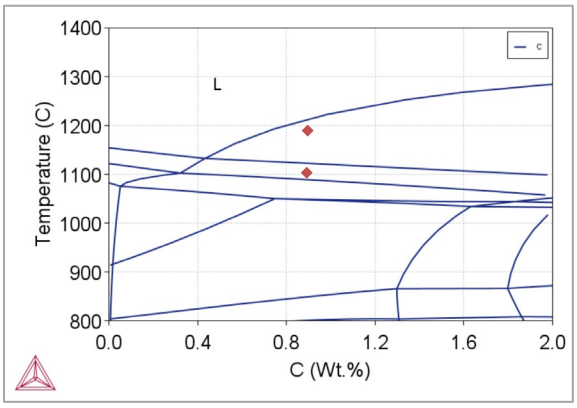

Figure 19. Calculated phase diagram of Stellite SF12, Co-base alloy with CC measurements (dots).

EAF STEELMAKING SLAG

Steelmaking is an energy intensive process that relies on fossil fuels to meet energy demands for primary extraction and refining of ores. The electric arc furnace (EAF) has the potential to significantly contribute to the decarbonization of the iron and steel industry. However, during EAF steelmaking, carbon must be injected into the molten slag to generate slag foaming, which is beneficial to the energy efficiency and protection of facility.[14] Most recently, our 100-kW induction melting furnace was utilized to simulate EAF steelmaking to study the slag foaming with carbon and biochar injection, as displayed in Fig. 20. The slag foaming is influenced by several variables such as slag composition, viscosity, surface tension, and temperature. In this work, the TA cup method was also utilized to measure the cooling curves of molten slag, as shown in Fig 21. The T_L was estimated as 1288C (2350F), and 1400C (2550F) for slag batches A and B, respectively. Obviously, the T_L of slag can also be determined using DTA (Fig. 22), 1405C (2560F), which is close to that of slag B tested in the TA cup (Fig. 21). No phase diagram was calculated for the nonmetallic compounds, EAF slag or LFP in this work.

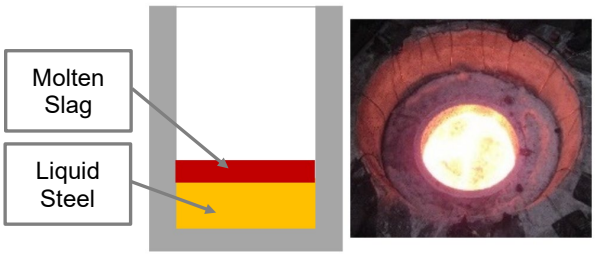

Figure 20. Left: A cross section of crucible in induction furnace, and right: Image of foamy slag during the melting experiment.

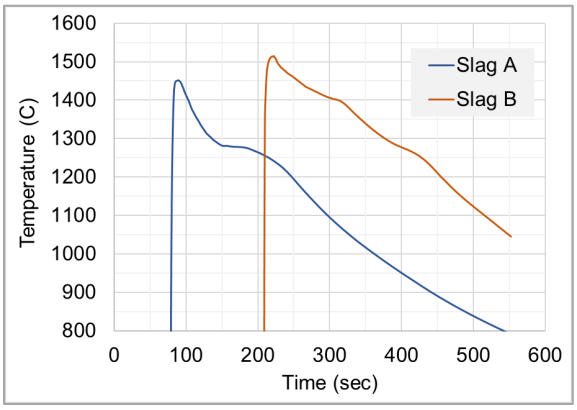

Figure 21. Measured cooling curves of EAF slag using the TA cup method.

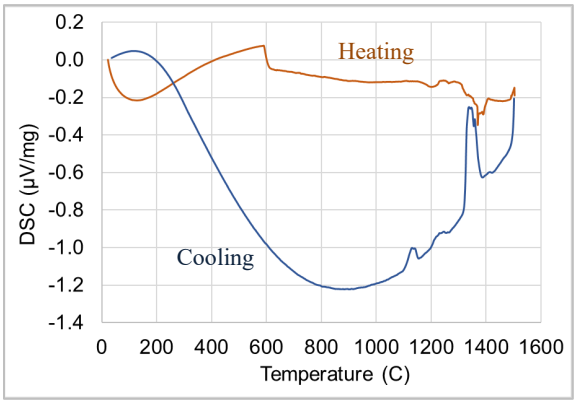

Figure 22. DTA curves of a slag sample.

LITHIUM IRON PHOSPHATE

The advantages of lithium iron phosphate $LiFePO_4$ as a cathode material include thermal stability, limited environmental impact and potential of low cost as compared to the cathode chemistries containing Co and Ni. Among many methods of synthesizing LFP, there are two processes at the industrial scale, solid state and hydrothermal. They require multiple, time-consuming steps and costly precursors. A group of Canadian researchers have developed a novel melt synthesis of LFP to reduce cost.[5,6] Melting cycle can be reduced using induction heating as compared to other methods. Nonmetallic charges usually cannot be directly heated by induction. In this work, a graphite crucible was utilized as susceptor to melt the inorganic precursors listed in Eqn. 1 as an example and synthesize LFP at a temperature of 1100C (2010F). A crushed piece of cast LFP ingot is shown in Fig. 23. The LFP castings were evaluated and compared against the commercial LFP product. Additional milling steps are required to reduce the cast LFP down to fine particles. Despite this drawback, the melt-synthesis has various advantages to produce LFP with much lower cost. A measured cooling curve is shown in Fig. 24. The T_L and T_S temperatures were determined as 1000C (1830F), and 880C (1615F),

respectively, which agree with the DTA testing results presented in Fig. 25. In contrast to the TA cup method, the DTA testing led to a large undercooling of □T=150C. The DTA testing was conducted using a small sample of 0.2 g and under scavenging of Ar gas flow, thus causing a largely undercooled LFP melt. For the TA cup and DTA methods, each one has its own advantages, e.g., foundry onsite testing for the former and two samples (to be tested and standard) controlled for the later.

$Fe_2O_3 + Fe + LiH_2PO_4 \square LiFePO_4$ Eqn. 1

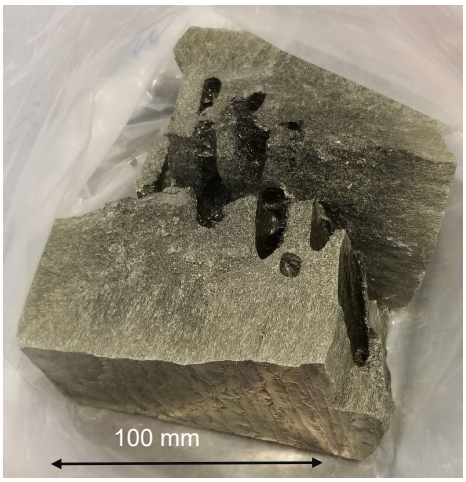

Figure 23. A crushed sample of cast LFP ingot.

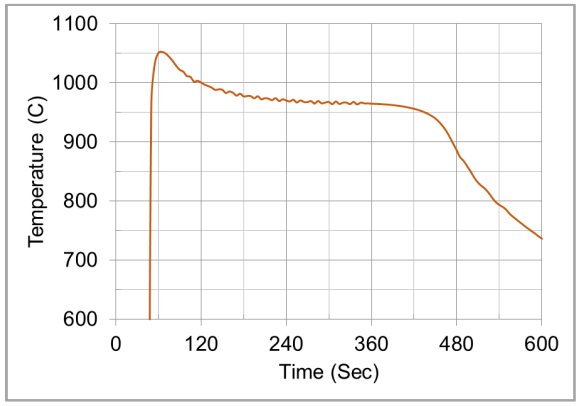

Figure 24. A measured cooling curve of LFP melt using the TA cup method.

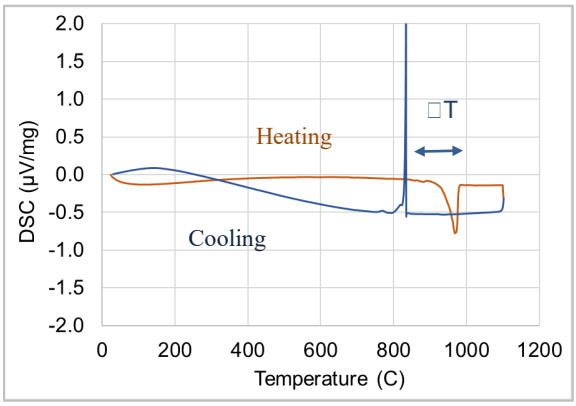

Figure 25. DTA curves of cast LFP sample showing T_L= 970C (1780F), T_S = 880C (1615F), and a large undercooling □T= 150C in solidification.

CONCLUSIONS

Cooling curves of metallic and nonmetallic melts were measured using the TA cup method and DTA, along with a brief review of these projects. The phase diagrams were calculated using Themo-Calc for the concentrated alloys including high-Si iron (14.5% Si), high-Mn (18% Mn) steel, Al-alloyed stainless steel, high-entropy alloy $AlCoCrFeNi_{2.1}$, Permalloy 80 Ni alloy, and Stellite Co alloy. The calculated results reasonably agreed with the TA cup measurements. In addition, our induction melting furnace was utilized to study steelmaking slag foaming and synthesize lithium iron phosphate. The liquidus temperatures determined from the TA cup method and DTA testing were close to each other in the present work.

ACKNOWLEDGMENTS

The work was performed at CanmetMATERIALS under the skillful and innovative contributions of P. Newcombe, H. Webster, D. Saleh, D. McFarlan, B. Ingram, B. Lacroix, G. Birsan, F. Benkel, J. Li, R. Zavadil, P. Liu, T. Smith, M. Aniolek, M. Podlesny, K. Sadayappan, A. Javaid, H. Jin, and C. DiGiovanni. The support of Canada OERD funding is gratefully acknowledged. The projects were performed in collaboration with industrial companies (Wescast Industries ON, Elkem, Kennametal ON, Anotec BC, ArcelorMittal Dofasco, Stelco, and Ignis Lithium), universities (University of British Columbia, University of Alberta, McMaster University, University of Montreal, Polytechnique Montreal, and University of New Hampshire), and other Canmet laboratories (CanmetENERGY and CanmetMINING). Thanks are also due to the reviewer(s) for the valuable comments and editing.

REFERENCES

1. Fredriksson, H., "Interpretation and Use of Cooling Curves (Thermal Analysis)," ASM Handbook, Volume 15, "Casting," ISBN 0-87170-007-7 (1998).
2. Stefanescu, D.M., "Thermal Analysis- Theory and Applications in Metalcasting" *AFS International Journal of Metalcasting, (IJMC)* 9, 7-22 (2015).
3. Tuttle, R.B., "In-Depth Analysis of Steel Cooling Curves," *2023 AFS Proc. of Metalcasting Congress*, Paper #23-066 (2023).
4. Solutions Fonderie (SFTA) thermal analysis for aluminum: solutionsfonderie.com/thermal-analysis/ (Link last accessed 04-03-2024.)
5. Gauthier, M., et al., "Melt Casting $LiFePO_4$: I. Synthesis and Characterization," *J. Electrochem. Soc.*, 157, A453-A462 (2010).
6. Sauriol, P., et al., "Fe^{3+} Reduction during Melt-Synthesis of $LiFePO_4$," *Canadian J. Chem. Eng.,* 97, 2196-2210 (2019).
7. Differential Thermal Analysis, Netzsch: DTA Testing Procedures Netzsch (Link last accessed 04-03-2024.)
8. High-Silicon Cast Iron Anode, https://anotec.com/ (Link last accessed 04-03-2024.)
9. Blair, M., et al. (ed.), "Steel Castings Handbook," 6th ed, SFSA and ASM Intl., ISBN 0-87170-226-7 (1995).
10. Field, K.G., et al., "Handbook on the Material Properties of FeCrAl Alloys for Nuclear Power Production Applications," U.S. DOE Report, M3FT-17OR020203031 (August 2017).
11. Lu, Y., *et al*., "A Promising New Class of High-Temperature Alloys: Eutectic High Entropy Alloys," *Sci. Rep*, Vol. 4, article # 6200, pp. 1-5 (2014).
12. Permalloy 80 Super Alloy, AZO Materials, www.azom.com (Link last accessed 04-03-2024.)
13. Stellite SF12: Kennametal.com/ca/en/. (Link last accessed 04-03-2024.)
14. DiGiovanni, C., *et al*., "Ranking of Injection Biochar for Slag Foaming Applications in Steelmaking," *Metals*, 13, 1003, 1-14 (2023).
15. "The Canadian Critical Minerals Strategy," From exploration to recycling: Powering the green and digital economy for Canada and the world. (2022). https://www.canada.ca/content/dam/nrcan-rncan/site/critical-minerals/Critical-minerals-strategyDec09.pdf (Link last accessed 01-11-2024.)
16. Li, L., "Rare Earth Extraction and Separation," Inner Mongolia Science and Technology Press, in Chinese, ISBN 978-7-5380-2052-6 (2011).
17. Davis, J.R., ASM Specialty Handbook, Cast Irons, ISBN 0-87170-564-8 (1999).
18. Foundry Handbook, Cast Iron, China Machine Press, in Chinese, ISBN 7-111-03117-2 (2002),
19. Havel, D., Austenitic Manganese Steel, A Complete Overview, Columbia Steel Casting Co., Inc. (Sept. 2017). (Link last accessed 01-11-2024.)
20. Li, D., *et al*., "Casting, Forging and Hot Rolling of High-entropy Alloy Ingots," 2023 AFS Proc. of Metalcasting Congress, Paper #23-010 (2023).
21. Bogno, A., *et al*., "Amorphous Phase Formation Analysis of Rapidly Solidified CoCr Droplets," *Metall. Mater. Trans. B* 47, 3257– 65 (2016).